

JGR Atmospheres

RESEARCH ARTICLE

10.1029/2018JD029592

Key Points:

- A new parameterization for the radiation-topography interaction is implemented to GCMs
- The interaction can increase the absorbed solar radiation at the surface
- Missing this effect in all CMIP5 models causes the systematic cold bias over the Tibetan Plateau

Correspondence to:

W.-L. Lee,
leelupin@gate.sinica.edu.tw

Citation:

Lee, W.-L., Liou, K.-N., Wang, C.-c., Gu, Y., Hsu, H.-H., & Li, J.-L. F. (2019). Impact of 3-D radiation-topography interactions on surface temperature and energy budget over the Tibetan Plateau in winter. *Journal of Geophysical Research: Atmospheres*, 124, 1537–1549. <https://doi.org/10.1029/2018JD029592>

Received 31 AUG 2018

Accepted 19 JAN 2019

Accepted article online 25 JAN 2019

Published online 14 FEB 2019

Author Contributions:

Conceptualization: Wei-Liang Lee, Kuo-Nan Liou, Chia-chi Wang, Yu Gu, Jui-Lin F. Li

Data curation: Wei-Liang Lee, Chia-chi Wang, Jui-Lin F. Li

Formal analysis: Wei-Liang Lee

Funding acquisition: Huang-Hsiung Hsu

Investigation: Wei-Liang Lee

Methodology: Wei-Liang Lee, Chia-chi Wang, Yu Gu, Huang-Hsiung Hsu, Jui-Lin F. Li

Resources: Wei-Liang Lee

Supervision: Kuo-Nan Liou, Huang-Hsiung Hsu

Validation: Wei-Liang Lee, Kuo-Nan Liou


Visualization: Wei-Liang Lee

Writing - original draft: Wei-Liang Lee

Writing - review & editing: Kuo-Nan Liou

©2019. American Geophysical Union.
All Rights Reserved.

Impact of 3-D Radiation-Topography Interactions on Surface Temperature and Energy Budget Over the Tibetan Plateau in Winter

Wei-Liang Lee¹ , Kuo-Nan Liou², Chia-chi Wang³ , Yu Gu² , Huang-Hsiung Hsu¹ , and Jui-Lin F. Li⁴ 

¹Research Center for Environmental Changes, Academia Sinica, Taipei, Taiwan, ²Joint Institute for Regional Earth System Science and Engineering and Department of Atmospheric and Oceanic Sciences, University of California, Los Angeles, CA, USA, ³Department of Atmospheric Sciences, Chinese Culture University, Taipei, Taiwan, ⁴Jet Propulsion Laboratory, California Institute of Technology, Pasadena, CA, USA

Abstract We incorporate a parameterization to quantify the effect of three-dimensional (3-D) radiation-topography interactions on the solar flux absorbed by the surfaces, including multiple reflections between surfaces and differences in sunward/shaded slopes, in the Community Climate System Model version 4 (CCSM4). A sensitivity experiment is carried out using CCSM4 with the prescribed sea surface temperature for year 2000 to investigate its impact on energy budget and surface temperature over the Tibetan Plateau (TP). The results show that the topographic effect reduces the upward surface shortwave flux and, at the same time, enhance snowmelt rate over the central and southern parts of TP. Comparing to observations and the ensemble of Coupled Model Intercomparison Project Phase 5 (CMIP5), we found that CMIP5 models have a strong cold bias of 3.9 K over TP, partially induced by the strong reflection of shortwave fluxes. We show that the inclusion of topographic effect reduces the substantial biases of upward shortwave fluxes and surface air temperatures over TP by 13% in the CCSM4 model.

Plain Language Summary We have developed a program to calculate the impact of shadow and multiple reflections on sunlight absorbed by the surface in mountainous areas for application to climate models. The results show that this impact can increase the amount of solar energy absorbed by the surface and produce a higher temperature. Because no climate model considers this effect currently, we believe it is why most global models severely underestimate the temperature over the Tibetan Plateau.

1. Introduction

The Tibetan Plateau (TP), with its high average elevation of 4.7 km and vast area of $2.4 \times 10^6 \text{ km}^2$, is the largest reservoir of frozen water in the world outside the Polar Regions, and therefore, it is referred as the third pole of the Earth (Qiu, 2008). TP has also been considered as a key factor in the formation of Indian summer monsoon (Molnar et al., 1993). It serves as a strong heat source in the middle troposphere during summer, which produces an anticyclonic circulation in the upper level over the South Asia. The circulation pattern leads to large-scale surface convergent flows toward the plateau, heavy precipitation along the southern slope of the Himalayas, and at the western coast of the Indian Peninsula and Bay of Bengal (Yanai & Wu, 2006; Wu et al., 2007, 2012). The massive glaciers and snowpack over TP and the intensive monsoon rainfall are the sources of major rivers, including Indus, Ganges, Brahmaputra, Mekong, Yangtze, and Yellow River, which supply fresh water to more than one billion people in East and South Asia.

It has been suggested that the extent of snow cover over TP could strongly influence the Indian summer monsoon through snow-albedo feedback (Blanford, 1884; Fasullo, 2004; Zhao & Moore, 2004). Therefore, an accurate quantification of surface albedo over complex topography is critical to the regional and global models in order to improve monsoon simulations. However, Brutel-Vuilmet et al. (2013) demonstrated that the multimodel mean of snow cover from the fifth phase of the Couple Model Intercomparison Project (CMIP5) has been overestimated over TP during the period of 1979–2005. Su et al. (2013) also reported that there are cold biases of $1.1^\circ\text{--}2.5^\circ\text{C}$ in the eastern part of TP in winter and spring from CMIP5 simulations during 1961–2005. Furthermore, Wei and Dong (2015) pointed out that the annual means of snow depth

in all CMIP5 models over TP are larger than those derived from in situ and satellite observations. These studies imply that an important physical process could be missing in most of state-of-the-art general circulation models (GCMs). For this reason, the melting rate of snow and glaciers on TP could be underestimated in projections of future climate, while the stress of water resources in East and South Asia could be more severe than that described in the Intergovernmental Panel on Climate Change 5th Assessment Report (2013).

In current weather or climate models, large biases of the shortwave flux could occur due to the neglect of topography and solar-beam interactions, particularly over snow covered mountains (Dozier, 1980; Dubayah et al., 1989). Due to the complexity of topography, which cannot be used as the lower boundary in plane-parallel radiative transfer schemes, Chen et al. (2006) and Lee et al. (2011) developed a Monte Carlo ray-tracing program to *exactly* simulate interactions between sunlight and rugged surfaces. On the basis of Monte Carlo simulations, Lee et al. (2011, 2013) further developed an innovative parameterization to adjust the downward solar flux for application to weather and climate models. This parameterization has been implemented into the Weather Research and Forecasting model and the Community Climate System Model version 4 (CCSM4). The objective is to demonstrate the impact of 3-D radiation-topography interactions on the surface energy budget and hydrology over the Sierra Nevada and Rocky Mountains in the western United States (Gu et al., 2012; Lee et al., 2015; Liou et al., 2013).

The topographic effect on clear-sky surface solar radiation over TP has been investigated using the above-mentioned approaches. Employing the Monte Carlo program with elevation data at a 1-km resolution, Liou et al. (2007) evaluated the surface downward solar flux and found that the deviations are 10–50 W/m² near Lhasa City of Tibet. Comparing to conventional radiative transfer calculations, the differences depend on the solar zenith angle and surface albedo. Lee et al. (2013) performed off-line calculations utilizing the parameterization developed for 10 × 10-km grid boxes over TP for the noon of the spring equinox. Deviations in the direct flux are on the magnitude of ±150 W/m² with positive values at the southern slopes and negative values at northern slopes and valleys. In addition, the deviations due to reflections could be more than 100 W/m² on the snow-covered regions, particularly along the Pamir and Himalaya Mountains. When the topography is smoothed into a coarse resolution such as 100 × 100 km for current GCMs, Lee et al. (2013) found that the positive/negative differences in surface solar radiation at sunward/shaded slopes of mountains could be evened out. Similarly, when a pixel is shadowed by nearby mountains and receives less sunlight, these nearby mountains would receive more, and this effect could also be smoothed out at a coarser resolution. In contrast, the surface-to-surface reflected flux always leads to additional surface absorption of solar radiation no matter what the resolution is. Therefore, the net effect of the radiation-topography interactions in a larger grid box is mostly increasing the total solar radiation absorbed by the surface and can exceed 20 W/m², indicating that the topographic effect remains important and should not be entirely ignored in climate simulations.

The objective of this study is to investigate the radiative impact of 3-D radiation-topography interactions on the surface temperature and energy budget over TP in winter using CCSM4 and incorporating in it the physical parameterization described above. This paper is organized as follows. In section 2, we briefly introduce the parameterization for the surface solar flux in mountains and CCSM4, as well as the ensemble data produced by GCMs participating in CMIP5 and the observation data used to evaluate model performance. The results of CCSM4 sensitivity test with and without the 3-D radiation and topography interactions are demonstrated in section 3. In section 4, the CMIP5 multimodel means are compared with observations and CCSM4 simulations. Concluding remarks are given in section 5.

2. Model Description, Experiment Design, and Reference Datasets

2.1. Parameterization for Surface Solar Flux in Mountains

The parameterization for surface solar flux adjustments has been based on a number of Monte Carlo simulations over the Sierra Nevada in the western United States (Lee et al., 2011). The deviation in the downward solar flux over a rugged surface, from that over a flat surface with the same mean elevation can be calculated by a set of linear regression equations with the sun's position and the following representative geographical parameters as input: slope, aspect, sky view factor, and terrain configuration factor. Using Shuttle Radar Topography Mission elevation data at a spatial resolution of 90 m, Lee et al. (2013) demonstrated that the topographical effect on the direct downward flux at the surface, including sunward and shaded slopes of

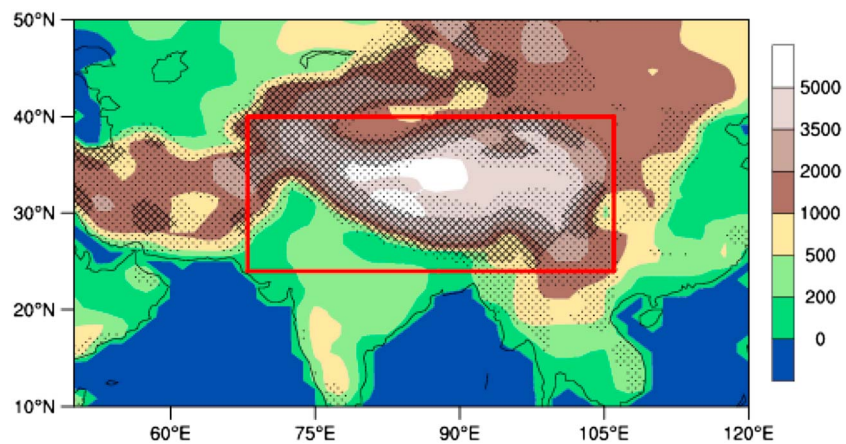


Figure 1. Elevation map of the Tibetan Plateau at a resolution of $0.95^\circ \times 1.25^\circ$. The red box indicates the region of interest within 24° – 40° N and 68° – 106° E. The dotted and hatched areas indicate the standard deviation of 1-km-resolution elevation within $0.95^\circ \times 1.25^\circ$ grid boxes are 200–400 m and larger than 400 m, respectively.

ranges and shadows cast by nearby mountains reaches maxima of $\pm 100 \text{ W/m}^2$ in *exact* Monte Carlo simulations. The reflected flux between land surfaces can be larger than 10 W/m^2 for a surface albedo of 0.1, and this flux is linearly proportional to albedo value. The topographic impact on the surface diffuse flux is generally less than 2 W/m^2 . The parameterization is able to explain more than 90% of the variations in direct and reflected fluxes in Monte Carlo simulations when the solar zenith angle is smaller than 75° .

This parameterization is further improved by adjusting the surface albedo instead of downward solar fluxes in CCSM4 to ensure consistencies of energy budget at the top of the atmosphere and between the atmosphere and land models (Lee et al., 2015). Surface albedo in GCM is basically determined by the land type, soil moisture, solar zenith angle, etc. However, we would like to point out that this model-derived albedo could be inaccurate over rugged surfaces. For example, a ray encountered two surface reflections will be attenuated to the square of albedo of its original energy, and the upward solar flux is smaller than that without considering the topographic effect. Therefore, surface albedo with the topographic adjustment should be closer to the *real* albedo, which could be observed by satellite.

2.2. NCAR CCSM4 and Sensitivity Experiments

CCSM4 was developed at the National Center for Atmospheric Research (NCAR, Gent et al., 2011), and it consists of the Community Atmosphere Model (CAM4), the Community Land Model (CLM4), the Community Ice Code for sea ice, and the Parallel Ocean Program. The dynamic core in CAM4 was based on the finite volume approach (Lin, 2004) with 26 vertical layers. The radiative transfer scheme in CAM4 was similar as in CAM3 (Collins et al., 2006), which utilizes the δ -Eddington approximation for shortwave radiation (Briegleb, 1992) and the absorptivity/emissivity formulation for longwave radiation (Ramanathan & Downey, 1986). For surface albedo calculations, CLM4 (Lawrence et al., 2011) included radiative transfer within vegetative canopy (Bonan, 1998; Dickinson, 1983), as well as within snow packs using the Snow and Ice Aerosol Radiation Model (Flanner & Zender, 2006).

To investigate the impact of topography-radiation interactions on surface temperature and energy budget over TP, we have carried out two CCSM4 simulations with the parameterization turned on and off, denoted as 3D and PP, respectively. The solar constant, sea surface temperature (SST), greenhouse gas concentrations, and aerosol loadings for year 2000 are prescribed in the simulations at a horizontal spatial resolution of $0.9^\circ \times 1.25^\circ$. The carbon-nitrogen feedbacks in CLM4 are enabled. The simulations have been run for 22 years from which the first 2 years are considered to be spin-up and discarded. Figure 1 is the elevation map of TP, defined as the areas with elevation higher than 2,000 m between 24° – 40° N and 68° – 106° E (marked as the red box) in this study. Also shown in the figure is the standard deviation of elevation at a resolution of 1 km within the $0.95^\circ \times 1.25^\circ$ CCSM4 grid boxes to represent the complexity of topography. The

Table 1
List of 30 Coupled Model Intercomparison Project Phase 5 Models Used for This Study

Model name	Resolution	Institute
ACCESS1.0	144 × 192	Commonwealth Scientific and Industrial Research Organization and Bureau of Meteorology, Australia
BCC-CSM1.1	64 × 128	Beijing Climate Center (BCC) and China Meteorological Administration, China
BNU-ESM	64 × 128	College of Global Change and Earth System Science, Beijing Normal University (BNU), China
CanCM4	64 × 128	Canadian Center for Climate Modeling and Analysis (CCCma), Canada
CanESM2	64 × 128	CCCma, Canada
CCSM4	192 × 288	National Center for Atmospheric Research (NCAR), United States
CESM1-BGC	192 × 288	NCAR, United States
CESM1-CAM5	192 × 288	NCAR, United States
CESM1-WACCM	192 × 288	NCAR, United States
CMCC-CM	240 × 480	Centro Euro-Mediterraneo per i Cambiamenti Climatici (CMCC), Italy
CNRM-CM5	128 × 256	Centre National de Recherches Meteorologiques (CNRM), France
FGOALS-g2	60 × 128	Institute of Atmospheric Physics, Chinese Academy of Sciences (IAP) and Tsinghua University (THU), China
FGOALS-s2	108 × 128	IAP and THU, China
GFDL-CM3	90 × 144	National Oceanic and Atmospheric Administration (NOAA) Geophysical Fluid Dynamics Laboratory (GFDL), United States
GFDL-ESM 2G	90 × 144	NOAA GFDL, United States
GFDL-ESM 2M	90 × 144	NOAA GFDL, United States
GISS-E2-H	90 × 144	National Aeronautics and Space Administration (NASA) Goddard Institute for Space Studies (GISS), United States
GISS-E2-R	90 × 144	NASA GISS, United States
HadCM3	73 × 96	Met Office Hadley Centre, United Kingdom
HadGEM2-CC	145 × 192	Met Office Hadley Centre, United Kingdom
HadGEM2-ES	145 × 192	Met Office Hadley Centre, United Kingdom
INM-CM4	120 × 180	Institute for Numerical Mathematics, Russia
IPSL-CM5A-LR	96 × 96	Institute Pierre-Simon Laplace (IPSL), France
IPSL-CM5A-MR	143 × 144	IPSL, France
MIROC4h	320 × 640	Japan Agency for Marine-Earth Science and Technology (JAMSTEC), Atmosphere and Ocean Research Institute, University of Tokyo (AORI), and National Institute for Environmental Studies (NIES), Japan
MIROC5	128 × 256	JAMSTEC, AORI, and NIES, Japan
MIROC-ESM	64 × 128	JAMSTEC, AORI, and NIES, Japan
MPI-ESM-LR	96 × 192	Max Planck Institute for Meteorology, Germany
MRI-CGCM3	160 × 320	Meteorological Research Institute, Japan
NorESM1-M	96 × 144	Norwegian Climate Center, Norway

Note. The resolution is presented in terms of the number of grid points (latitude × longitude).

areas with large standard deviations of elevations generally locate at the margin of TP and several mountain ranges, while the central part of the plateau is relatively flat.

2.3. CMIP5 Ensembles

We select 30 simulations from different models or model configurations in the CMIP5 archive as listed in Table 1. To compare with available observation data and our sensitivity tests, the coupled atmosphere-ocean simulations from 1850 to 2005 with the historical greenhouse gases, ozone, aerosols, and solar constant are used (Taylor et al., 2012), and we utilize the data covering the period 1995–2005 for this study. Variables to be evaluated are the near surface air temperature, the surface downward shortwave flux (FSDS), and the surface upward shortwave flux (FSUS). All model outputs are regridded to a spatial resolution of 2°, and the ensemble means are then calculated.

2.4. Observational Data

We have used the University of Delaware (UDel) terrestrial air temperature monthly gridded data sets, which are data compiled from a large number of station records (Willmott & Matsuura, 1995) at a spatial

resolution of $0.5^\circ \times 0.5^\circ$ for the period 1901 to 2014. We have also regridded the data of version 4.01 covering 1995 to 2005 to the same resolution as the CMIP5 ensemble for comparison purposes.

To evaluate the surface solar radiation in CMIP5 ensemble and CCSM4 simulations, we utilize downward and upward shortwave fluxes at the surface from the Clouds and the Earth's Radiant Energy System-Energy Balanced and Filled (CERES-EBAF, Kato et al., 2018). Using the top-of-atmosphere irradiance measured by CERES and cloud properties derived from the Moderate Resolution Imaging Spectroradiometer, CloudSat, and Cloud-Aerosol Lidar and Infrared Pathfinder Satellite Observations as inputs, surface fluxes are obtained by carrying out radiative transfer calculation at a 1° resolution. For our study, we have used the Edition 4 data covering the period 2000 to 2005. The uncertainties of CERES-EBAF all-sky surface shortwave radiation are 3 and 4 W/m^2 for upward and downward radiation, respectively. However, uncertainties could be up to 10 W/m^2 over TP as shown by Figure 7 in Kato et al. (2018).

3. Results of CCSM4 Sensitivity Test

3.1. Impact on Snowpack

Figures 2a–2d display the net surface solar flux (FSNS), clear-sky net surface solar flux (FSNSC), cloud cover, and snow cover for the PP case, respectively, over TP in the winter season (December, January, and February, DJF). FSNS (Figure 1a) is primarily determined by cloud cover, surface albedo, and latitude so that the minimum of FSNS occurs at the northwestern part of TP along with a large snow cover and cloud cover at the northern part of TP. The snow cover (Figure 2d) is generally larger than 90% in the western part of TP, whereas it is smaller in the eastern region due to higher temperature and less snowfall. We find that the spatial pattern and magnitude of FSNS and FSNSC (Figures 2a and 2b) are extremely similar even in the regions with large cloud covers (Figure 2c). For example, the difference between FSNS and FSNSC in the area of Kashmir, where the cloud cover is generally larger than 45%, is smaller than in the southeastern corner of TP with the cloud cover less than 25%. Two possible reasons cause the smaller effect by clouds. First, because the regions with large cloud cover generally located at areas with large snow cover, the presence of clouds over reflected surface will decrease the direct flux but increase multiple reflections between cloud and surface. Second, larger cloud covers generally exist in high elevation areas over TP. For this reason, cloud depths are both spatially and optically smaller, leading to smaller differences between FSNS and FSNSC.

Figures 2e–2h show deviations in FSNS, FSNSC, cloud cover, and snow cover between 3D and PP simulations (3D-PP), respectively. The snow cover (Figure 2h) decreases in most inland areas of TP in 3D simulations; however, the reduction along the Himalayas is not significant. The FSNSC deviation (Figure 2f) generally follows the pattern of snow cover deviation, but in opposite sign. FSNSC increases significantly along the Himalayas, indicating the contribution from the 3-D topographic effect such that the southern slope of the Himalayas receives more direct solar radiation in winter than in conventional GCMs. Deviations in FSNS and FSNSC (Figures 2e and 2f) are almost the same since the cloud cover deviation (Figure 2g) is generally very small and statistically insignificant. The snow cover decreases over most of TP as expected because the topography-radiation interaction can increase the surface net solar radiation by including reflected fluxes (Lee et al., 2013). We note that positive-negative pairs of flux deviations on the sunward and shaded sides of mountains might be compensating each other over a larger domain.

To further demonstrate the impacts of the topography-radiation interactions on the snowpack over TP, Figures 3a–3c show the snow water equivalent, snowfall rate, and snowmelt rate of the PP case in DJF, respectively. While the snow cover (Figure 2d) is close to 100% in the western part of inland TP, the snow water equivalent (Figure 3a) in this region is much smaller than in the Pamir, Karakoram, and Himalaya Mountains because most snowfall (Figure 3b) occurs at the southwestern boundary of TP. Significant snowmelt (Figure 3c) occurs primarily along Himalaya Mountains.

The corresponding deviations in snow water equivalent, snowfall rate, and snowmelt rate (3D-PP) are shown in Figures 3d–3f, respectively. The snow water equivalent (Figure 3d) decreases significantly in the western part of TP, particularly along the Himalayas where it could reduce by 40%, while the change is small in the eastern part. The change in snow water equivalent is determined by the rates of snowfall and snowmelt. Both are favorable to the reduction in snowpack, as shown in Figures 3e and 3f. Although the

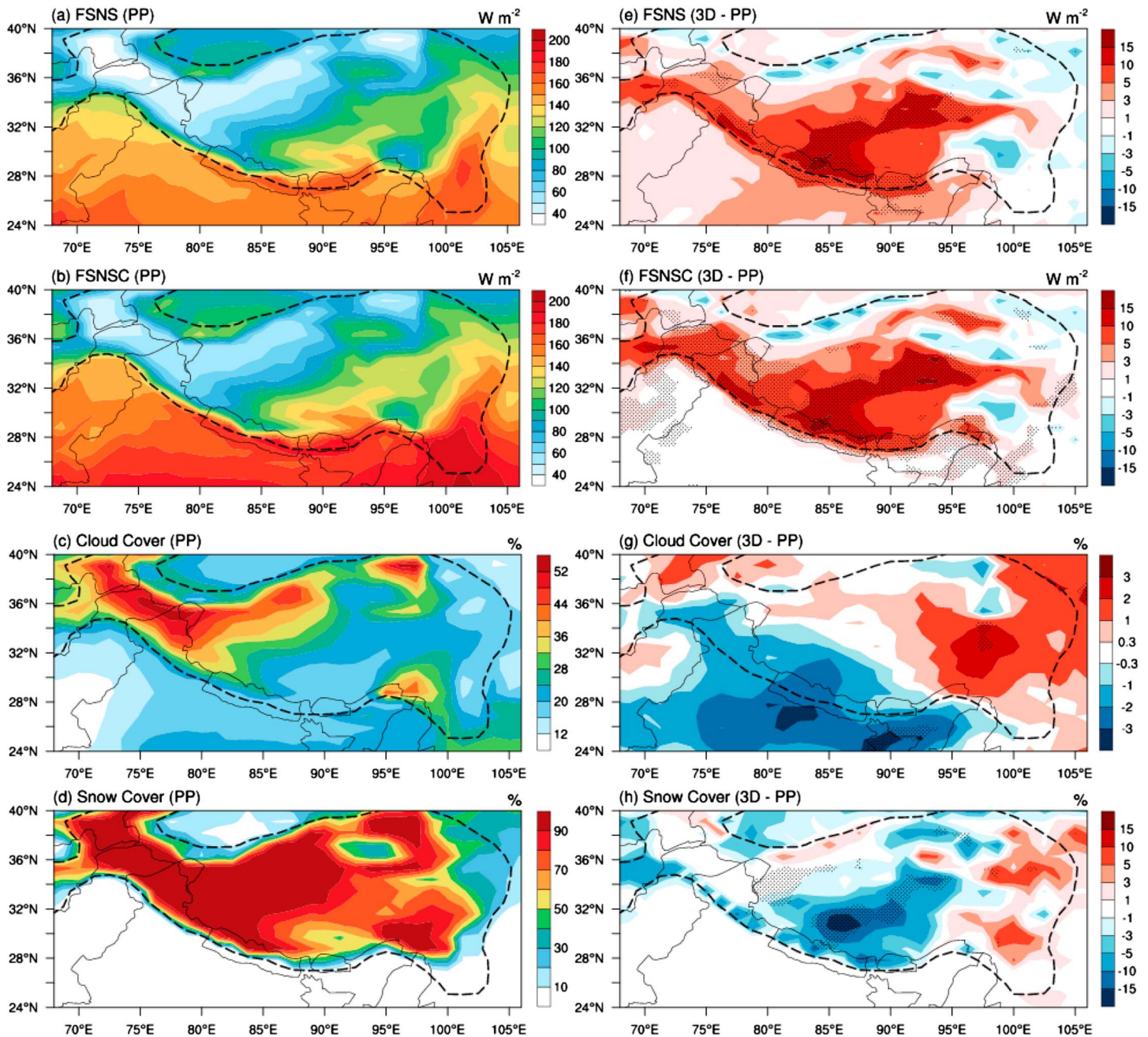


Figure 2. Twenty-year averages of (a) surface net solar flux (FSNS), (b) clear-sky surface net solar flux (FSNSC), (c) cloud cover, and (d) snow cover for PP case, as well as the differences in (e) FSNS, (f) FSNSC, (g) cloud cover, and (h) snow cover between 3-D and PP cases (3-D-PP). The dotted areas denote the differences are significant at the 95% level, and the dashed lines indicate the 2,000-m contour line.

snowfall rate decreases along the Himalayas, its maximal magnitude, about -0.5 mm/day, is not significant. In contrast, the snowmelt rate deviation is more than 0.8 mm/day, which is statistically significant and indicates that the enhanced snowmelt caused by topography-radiation interactions is the main factor in snowpack reduction along the Himalayas. The weather systems in the two cases differ due to altered surface forcing; however, the resulting snowfall decrease in the 3D case does not contribute significantly to the change in snow water equivalent. Because the amount of snow available for melting is very small in the 3D case, the snowmelt rate is significantly smaller in the 3D case over inland TP and the region near Bhutan when a smaller snow water equivalent occurs.

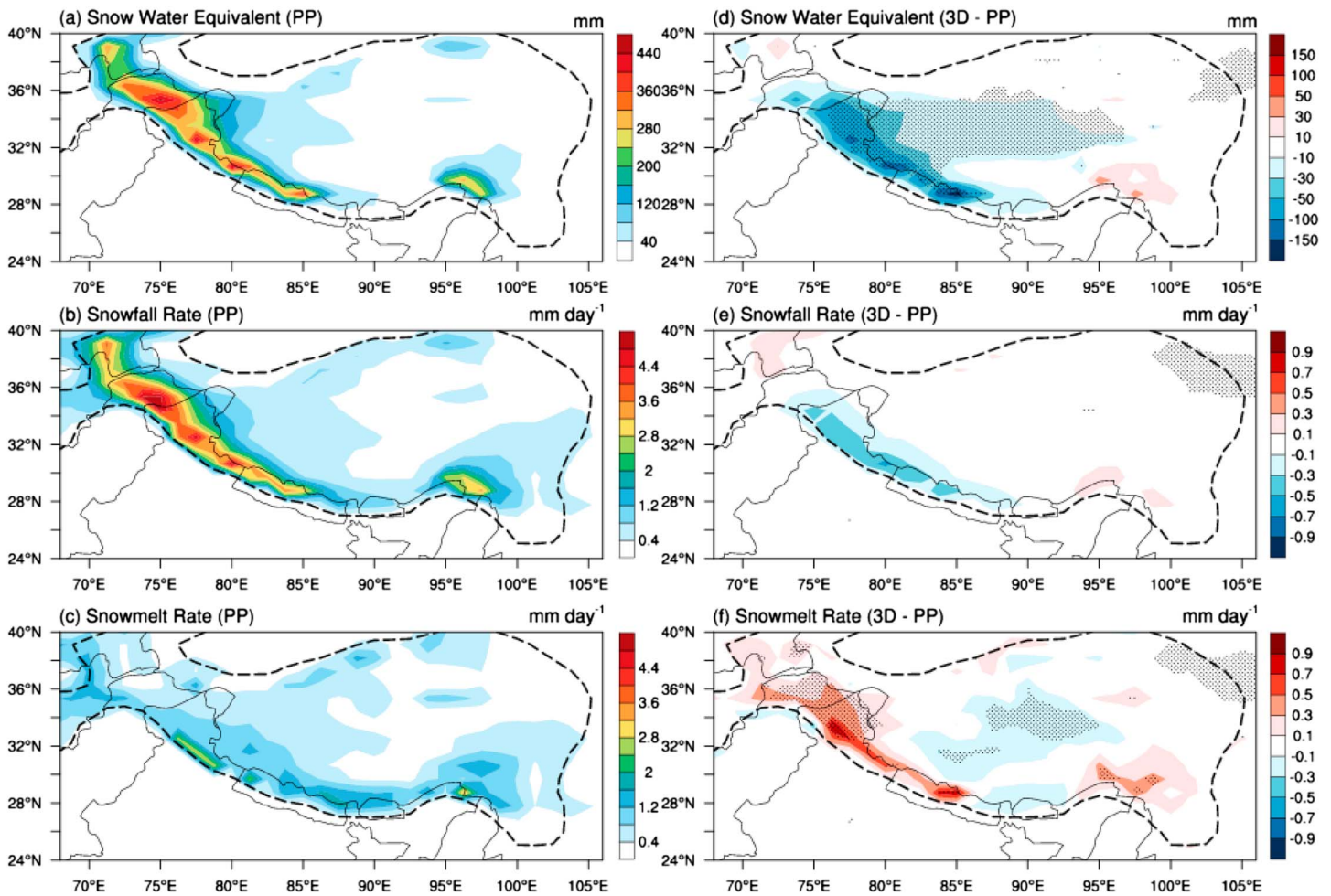


Figure 3. Twenty-year averages of (a) snow water equivalent, (b) snowfall rate, and (c) snowmelt rate for PP case, as well as the differences in (d) snow water equivalent, (e) snowfall rate, and (f) snowmelt rate between 3-D and PP cases (3-D-PP). The dotted areas denote the differences are significant at the 95% level, and the dashed lines indicate the 2,000-m contour line.

3.2. Impact on Land Surface Temperature and Energy Budget

The land surface temperature (T_s) can be calculated by the energy budget at the surface using Stefan-Boltzmann law (Li et al., 2016):

$$\varepsilon\sigma T_s^4 = \text{RSDS} - \text{RSUS} + \varepsilon\text{RLDS} - \text{SHFX} - \text{LHFX} - \text{GHFX} \quad (1)$$

where ε is the surface longwave radiation emissivity, σ is the Stefan-Boltzmann constant, RSDS and RSUS are the downward and upward shortwave fluxes at the surface, respectively, RLDS is the downward longwave flux, SHFX and LHFX denote the sensible and latent heat fluxes, respectively, and GHFX represents the ground heat flux. GHFX can be further decomposed into the heat flux of snowmelt and the heat flux into the ground. The latter is negligible in long-term average. Emissivity is close to unity for land surfaces and was used in the following analysis.

Figure 4a displays the difference in T_s between 3D and PP cases consistent with the FSNS difference, as shown in Figure 2e, that inland areas are warmer due to absorbing more solar radiation. Also, the plain along the Ganges River is much warmer in the 3D case. However, the T_s deviation along the Himalayas in Nepal is close to zero even though the FSNS difference is largest, implying that the additional energy must be balanced by other form of energy fluxes.

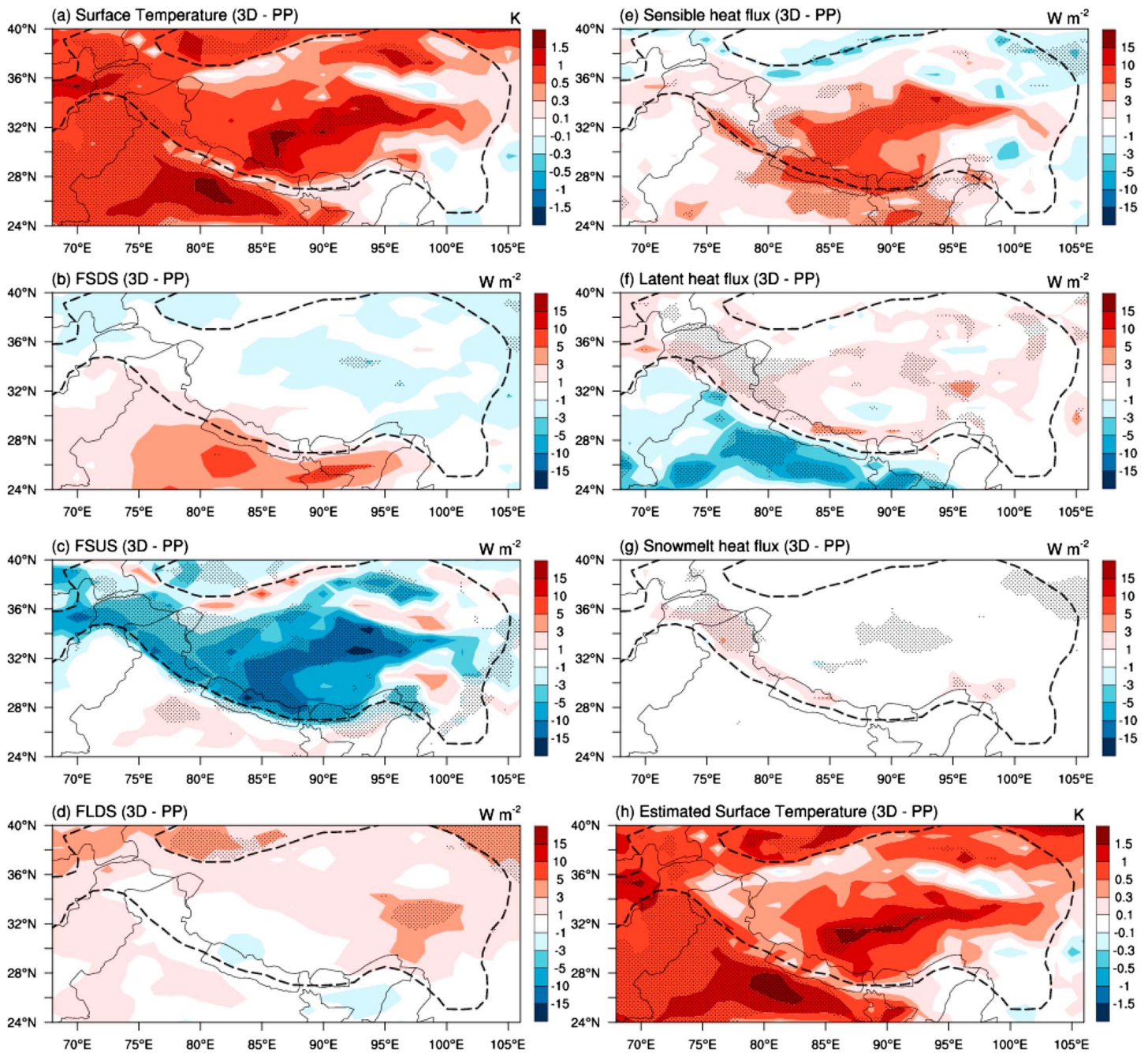


Figure 4. Twenty-year averages of differences in (a) surface temperature, (b) surface downward solar flux (FSDS), (c) surface upward solar flux (FSUS), (d) surface downward longwave flux (FLDS), (e) sensible heat flux, (f) latent heat flux, (g) snowmelt heat flux, and (h) estimated surface temperature using equation (1) between 3D and PP cases (3D-PP). The dotted areas denote the differences are significant at the 95% level, and the dashed lines indicate the 2,000 m contour line.

Figures 4b to 4g show differences in each term on the right-hand side of equation (1) between 3D and PP cases. The FSDS difference is within $\pm 3 \text{ W/m}^2$, which is insignificant over most of TP because the difference in cloud cover is small (Figure 2g). However, FSUS in the 3D case is much smaller than in the PP case, and the difference could be more than 15 W/m^2 in the central part of TP and along the Himalayas, indicating that the surface absorbs more solar radiation in the 3D case due to less reflection. FLDS is generally controlled by the near-surface air temperature and the temperature of the cloud base above. Also comparing to Figure 2g, we find that the difference in FLDS is primarily determined by a larger cloud cover, resulting in emitting more downward longwave radiation to the surface. For this reason, the FLDS difference is

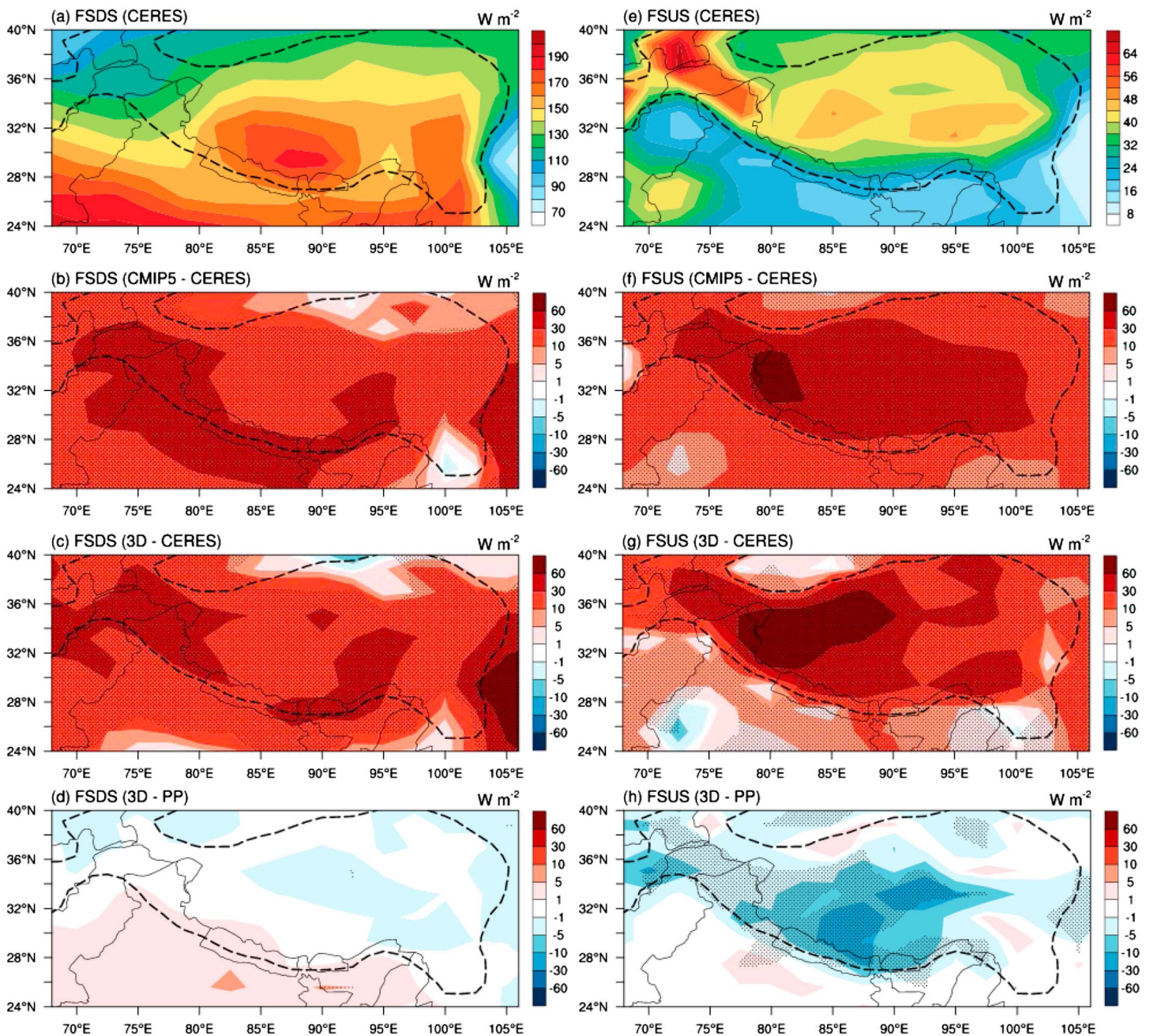


Figure 5. FSDS for (a) CERES-EBAF remote sensing, (b) difference between CMIP5 ensemble mean and CERES-EBAF (CMIP5-CERES), (c) difference between 3D case and CERES-EBAF (3D-CERES), and (d) difference between 3D case and PP case (3D-PP), as well as FSUS for (e) CERES-EBAF remote sensing, (f) difference between CMIP5 ensemble mean and CERES-EBAF (CMIP5-CERES), (g) difference between 3D case and CERES-EBAF (3D-CERES), and (h) difference between 3D case and PP case (3D-PP). The dotted areas denote the differences are significant at the 95% level, and the dashed lines indicate the 2,000-m contour line. FSDS = surface downward solar flux; FSUS = surface upward solar flux; CERES-EBAF = Clouds and the Earth's Radiant Energy System-Energy Balanced and Filled; CMIP5 = Coupled Model Intercomparison Project Phase 5.

insignificant because the cloud cover difference is very small. The magnitude of the difference in the sensible heat flux is larger than the latent heat flux and the snowmelt heat flux, revealing that most of the additional energy received by the surface in the 3D case due to a smaller FSUS is compensated by the sensible heat flux. The latent heat flux is also larger over TP in the 3D case, probably because more water is available for evaporation from enhanced snowmelt. However, the latent heat flux is significantly smaller in the 3D case in the plain area south of the Himalayas, implying a dryer and warmer Gangetic

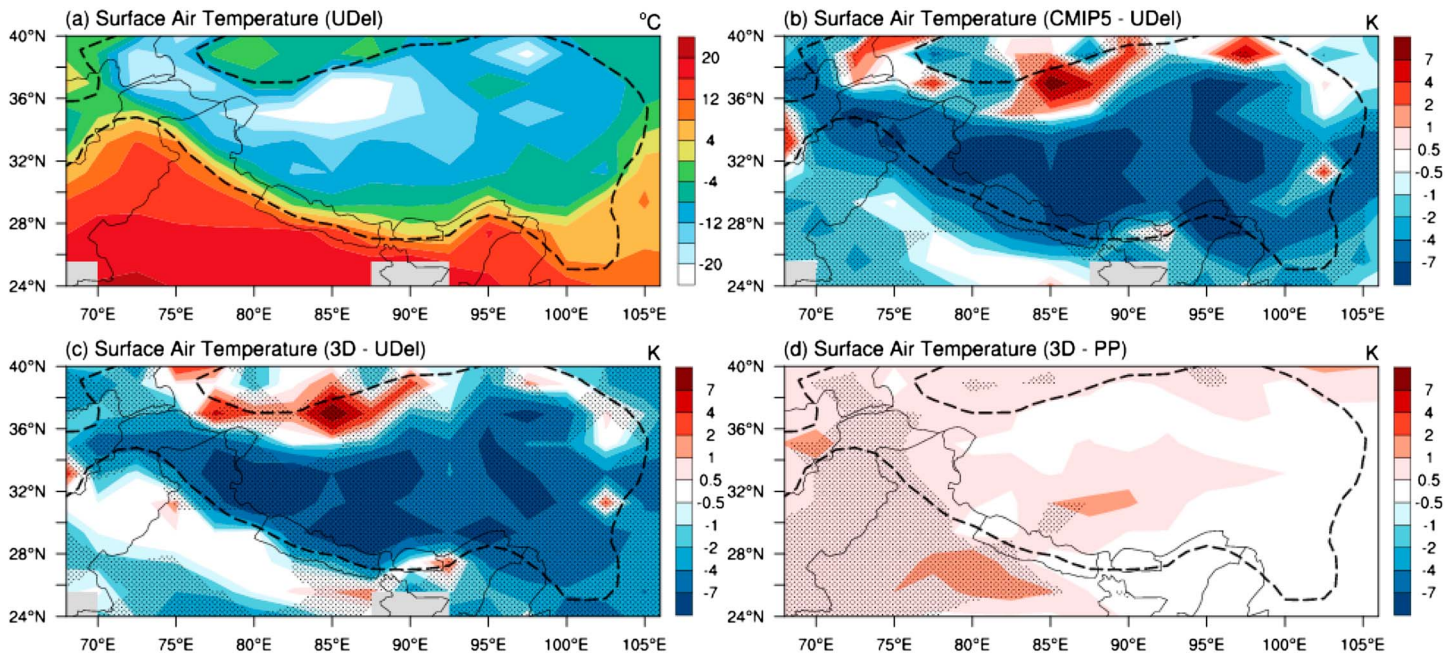


Figure 6. Surface air temperature for (a) analysis data from University of Delaware (UDel), (b) difference between Coupled Model Intercomparison Project Phase 5 (CMIP5) ensemble mean and UDel (CMIP5-UDel), (c) difference between 3D case and UDel (3D-UDel), and (d) difference between 3D case and PP case (3D-PP). The dotted areas denote the differences are significant at the 95% level, and the dashed lines indicate the 2,000-m contour line.

Plain in winter. While the heat flux from snowmelt is significantly larger in the 3D case over Karakoram Mountains and the inland area of TP, the difference between the two cases is less than 3 W/m^2 , smaller than sensible and latent heat fluxes.

By summing up all terms on the right hand side of equation (1), we can estimate the surface temperatures of the PP and 3D cases using the Stefan-Boltzmann law. Figure 4h displays the difference in estimated surface temperature, which is consistent with the difference in the real surface temperature between the two cases shown in Figure 3a. It follows that the surface temperature difference over TP between the two cases can be explained by surface energy fluxes. FSUS is the most important factor, while sensible and latent heat fluxes are the response to the additional solar energy. This energy budget analysis reveals that the inclusion of 3-D radiation-topography interactions in GCM simulations can effectively increase surface temperature in TP by reducing upward solar fluxes.

4. Comparison With Observations and CMIP5 Multimodel Mean

Figures 5a–5d show FSDS determined from CERES-EBAF, and their differences between CERES-EBAF and CMIP5 ensemble, CERES-EBAF and the 3D case, and 3D and PP cases, respectively. CMIP5 ensemble overestimates FSDS over the whole TP, particularly along the Himalayas where the bias is larger than 30 W/m^2 . This bias also exists in the 3D case but with a smaller magnitude. It is noted that the biases in CMIP5 ensemble and 3D case are much larger than the uncertainties of CERES-EBAF, which are up to 10 W/m^2 over TP. Figure 4d shows that the difference between 3D and PP cases is generally smaller than 2 W/m^2 (see also Figure 4b) because cloud cover differences are small (Figure 2g). Although the FSDS bias in the 3D case is smaller than in the PP case (Figure 4b), however, the inclusion of radiation-topography interactions in CCSM4 does not show to improve the FSDS bias over TP.

Figures 5e–5h illustrate FSUS from CERES-EBAF and their FSUS differences between CERES-EBAF and CMIP5 ensemble, CERES-EBAF and the 3D case, and between 3D and PP cases, respectively. The CMIP5 ensemble strongly overestimates FSUS by more than 30 W/m^2 over most TP areas with deviations reaching 60 W/m^2 near Karakoram Mountains. The magnitude of the bias is larger than FSDS, indicating that the positive FSUS bias is not contributed by excessive FSDS only. On the contrary, FSUS bias in the 3D case is

Table 2

Spatial Averages of the Surface Downward Solar Flux (FSDS), Surface Upward Solar Flux (FSUS), Surface Net Solar Flux (FSNS), Surface Albedo, and Air Temperature at 2-m Above Surface (Surface Air Temperature, SAT) of Observation (Clouds and the Earth's Radiant Energy System-Energy Balanced and Filled for Radiative Fluxes and Albedo and University of Delaware for SAT), Coupled Model Intercomparison Project Phase 5 (CMIP5) Ensemble Means, and Community Climate System Model Version 4 (CCSM4) Simulations with and Without the Topographic Effect (3D and PP). The Domain is the Tibetan Plateau with Elevation Over 2,000 m in the Box of 24°–40°N and 68°–106°E, as Shown as the Area Within the Thick Dashed Line in Figure 2

Variables	Observation	CMIP5	3D	PP
FSDS (W/m^2)	146.5	168.8	171.9	172.4
FSUS (W/m^2)	38.2	72.8	73.0	77.1
FSNS (W/m^2)	108.3	96.0	98.9	95.3
Surface albedo	0.26	0.43	0.42	0.45
SAT ($^{\circ}\text{C}$)	−8.7	−12.6	−12.8	−13.3

smaller in the eastern part of TP, but the bias is larger than 60 W/m^2 in the most region of western TP. While FSUS in the 3D case has larger bias than CMIP5 ensemble, Figure 4h reveals that the inclusion of radiation-topography interactions can substantially improve FSUS in CCSM4 simulations by more than 10 W/m^2 over the central TP and the Himalayas (see Figure 4c).

Figures 6a–6d show the surface air temperature (SAT) from UDel and SAT differences between UDel and CMIP5 ensemble, between UDel and the 3D case, and between 3D and PP cases, respectively. The cold bias of CMIP5 ensemble is larger than 7 K over the central and southern parts of TP, whereas a strong warm bias exists at the northern edge of TP. In the 3D case, the magnitude and spatial distribution of SAT biases are similar to CMIP5 ensemble. The SAT difference between 3D and PP cases shown in Figure 6d is similar to the surface temperature difference depicted in Figure 4a, which leads to improvement by more than 1 K in the central TP where the cold bias is the largest.

Table 2 lists the domain-averaged FSDS, FSUS, surface and SAT over the region with altitudes higher than 2,000 m, as shown in Figures 5 and 6 within the area circled by the dashed line, for observation data (radiation and albedo from CERES-EBAF and SAT from UDel), CMIP5 ensemble, and 3D and PP cases. FSDS is overestimated by 24 W/m^2 for CMIP5 ensemble over TP, and this bias is larger in CCSM4. While the 3D case performs better than the PP case, the improvement is only 0.5 W/m^2 and insignificant. The FSUS bias in CMIP5 ensemble is about 34 W/m^2 , which is worse than FSDS bias due to overestimated surface albedo such that too much snow remaining over TP. The FSUS bias in the PP case is worse than that in CMIP5 ensemble, but with the implementation of radiation-topography interactions, the bias is significantly improved by 4 W/m^2 in the 3D case.

Although too much sunlight reaches the surface in the CMIP5 ensemble, there is even more shortwave radiation reflected back to the space. Consequently, the FSNS in CMIP5 models is 12 W/m^2 smaller than the observations—the main reason that a strong cold bias of 3.9 K exists over TP. The FSNS biases in PP and 3D cases are 13.0 and 9.4 W/m^2 , respectively. The improved FSNS in the 3D case also lead to a smaller cold bias of 4.1 K comparing to 4.6 K in the PP case, which represents a 13% temperature improvement, significant at a 95% confidence level.

It is noted that the SST in our sensitivity test is prescribed and differs from CMIP5 ensembles, which are coupled with dynamic ocean models. However, the spatial biases patterns in FSDS, FSUS, and SAT over TP in CCSM4 are close to CMIP5 ensembles, implying that CCSM4 results are reasonable to represent the general characteristics of the preceding biases over TP. Therefore, it is most likely that the improvement shown in the 3D case would also take place in CMIP5 models if radiation-topography interactions are included.

5. Concluding Remarks

We have implemented the parameterization of 3-D radiation-topography interactions in CCSM4 to accounting for the impacts of reflections between mountains and differences in sunny/shaded slopes on solar radiation absorbed by the surface. The sensitivity experiments using CCSM4 have been carried out with a prescribed SST of year 2000 at a resolution of $0.9^{\circ} \times 1.25^{\circ}$. The simulations with the parameterization turned on (3D) and off (PP) have been run for 22 years, and we use the outputs in winters (DJF) of the last 20 years for analysis.

The results reveal that the topographic effect can cause an increase in the FSNS in the central and southern part of TP. Because the cloud cover difference is small over most of TP, the FSNS increase is directly related to albedo reduction due to a smaller snow cover. The decreases in snow cover and snow water equivalent along the Himalayas are primarily caused by the increase in snowmelt rate due to additional direct radiation at the sunward slope, but the contribution from the snowfall rate reduction is small. Analysis of the surface energy budget demonstrates that the decrease in the upward surface solar flux (FSUN) in the 3D case is the

main factor to induce warmer surface temperature in the central and southern parts of TP, without significant changes in downward shortwave and longwave radiation fluxes. The warmer land surface over TP causes larger sensible and latent heat fluxes, as well as increased snowmelt.

The CCSM4 simulations are also compared with CMIP5 multimodel ensemble results and observations, including surface radiation from CERES satellite remote sensing and surface air temperature analysis data from the UDel. CMIP5 models, including CCSM4, allow too much solar radiation reaching the surface, especially along the Himalayas with a bias more than 20 W/m^2 . On the other hand, the bias of the upward shortwave flux, with the mean and maximum values of 34 W/m^2 and 73 W/m^2 , respectively, is larger than the bias of the downward shortwave flux in CMIP5 ensemble. The resulting FSNS bias of -12 W/m^2 appears to be the main factor causing a -3.9 K surface air temperature bias over TP. The CCSM4 sensitivity experiment shows that the inclusion of the 3-D topographic effect improves the mean upward shortwave flux bias by 4.1 W/m^2 by accounting for multiple reflections and differences over sunward and shaded slopes leading to the reduction of cold bias by 0.5 K in the 3D case, equivalent to a 13% improvement in surface air temperature.

Although the inclusion of 3-D radiation-topography effect can significantly improve temperature simulations over the Tibetan Plateau, other physical processes missing in most of the GCMs could also contribute to the cold bias. For example, Liou et al. (2014) reported that the internal mixing of black carbon or dust with snow and multiple inclusions of black carbon/dust in a snow grain can substantially reduce albedo of snow surfaces. However, this effect is not incorporated by current climate models yet, and it could lead to cold bias over the Tibetan Plateau due to enormous emission from East and South Asia. It is also known that snow is a diagnosed variable and has no interaction with radiation in most CMIP5 models. Li et al. (2016) show that the lack of the radiative effect of precipitating snow in the air would underestimate the downward longwave radiation and therefore could result in cold bias in most of land surface in the winter hemisphere. In addition, missing of these physical processes may have nonlinear effects and further deteriorates GCM simulations.

In view of the above, the 3-D radiation-topography effect is an important physical process critical to the surface energy budget over areas with complex terrain. Finally, since this effect is not accounted for in all of current GCMs, we submit that the warming and snowmelt rates over TP have been underestimated and could result in inaccurate and/or erroneous projections of hydrology, water resources, and South Asia monsoon over the vast TP and surrounding areas.

Acknowledgments

The contribution from W.-L. Lee, C.-c. Wang, and H.-H. Hsu to this study is supported by Ministry of Science and Technology of Taiwan under contracts MOST 106-2111-M-001-002, MOST 106-2111-M-034-002, and MOST 106-2111-M-001-005. K.-N. Liou and Y. Gu are supported by NSF grant AGS-1660587. For J.-L. F. Li, the research was carried out at the Jet Propulsion Laboratory, California Institute of Technology, under a contract with the National Aeronautics and Space Administration (NASA). The surface solar fluxes are CERES-EBAF obtained from https://ceres.larc.nasa.gov/order_data. The surface air temperature over land (UDeI) can be retrieved at https://www.esrl.noaa.gov/psd/data/gridded/data/UDeI_AirT_Precip.html. The land surface temperature is Level-3 gridded monthly data from MODIS at <https://landval.gsfc.nasa.gov/ProductStatus.php?ProductID=MOD11>. CMIP5 data can be downloaded from https://cmip.llnl.gov/cmip5/data_portal.html. The simulation data using CCSM4 with and without the parameterization are available at <ftp://140.109.172.47/pub/lupin/3D-RT/CCSM4>.

References

- Blanford, H. F. (1884). On the extension of the Himalaya snowfall with dry winds and seasons of drought in India. *Proceedings of the Royal Society*, *37*, 3–22.
- Bonan, G. B. (1998). The land surface climatology of the NCAR Land Surface Model coupled to the NCAR Community Climate Model. *Journal of Climate*, *11*(6), 1307–1326. [https://doi.org/10.1175/1520-0442\(1998\)011<1307:TLSCOT>2.0.CO;2](https://doi.org/10.1175/1520-0442(1998)011<1307:TLSCOT>2.0.CO;2)
- Briegleb, B. P. (1992). Delta-Eddington approximation for solar radiation in the NCAR Community Climate Model. *Journal of Geophysical Research*, *97*, 7603–7612. <https://doi.org/10.1029/92JD00291>
- Brutel-Vuilmet, C., Ménégoz, M., & Krinner, G. (2013). An analysis of present and future seasonal Northern Hemisphere land snow cover simulated by CMIP5 coupled climate models. *The Cryosphere*, *7*(1), 67–80. <https://doi.org/10.5194/tc-7-67-2013>
- Chen, Y., Hall, A., & Liou, K. N. (2006). Application of 3D solar radiative transfer to mountains. *Journal of Geophysical Research*, *111*, D21111. <https://doi.org/10.1029/2006JD007163>
- Collins, W. D., Rasch, P. J., Boville, B. A., Hack, J. J., McCaa, J. R., Williamson, D. L., et al. (2006). The formulation and atmospheric simulation of the Community Atmosphere Model Version 3 (CAM3). *Journal of Climate*, *19*, 2144–2161.
- Dickinson, R. E. (1983). Land surface processes and climate-surface albedos and energy balance. *Advances in Geophysics*, *25*, 305–353. [https://doi.org/10.1016/S0065-2687\(08\)60176-4](https://doi.org/10.1016/S0065-2687(08)60176-4)
- Dozier, J. (1980). A clear-sky spectral solar radiation model for snow-covered mountainous terrain. *Water Resources Research*, *16*, 709–718. <https://doi.org/10.1029/WR016i004p00709>
- Dubayah, R., Dozier, J., & Davis, F. W. (1989). The distribution of clear-sky radiation over varying terrain. *Proceedings IGARSS '89, volume 2*, pp. 885–888, IEEE 89CH2768-0.
- Fasullo, J. (2004). A stratified diagnosis of the Indian monsoon–Eurasian snow cover relationship. *Journal of Climate*, *17*(5), 1110–1122. [https://doi.org/10.1175/1520-0442\(2004\)017<1110:ASDOTI>2.0.CO;2](https://doi.org/10.1175/1520-0442(2004)017<1110:ASDOTI>2.0.CO;2)
- Flanner, M. G., & Zender, C. S. (2006). Linking snowpack microphysics and albedo evolution. *Journal of Geophysical Research*, *111*, D12208. <https://doi.org/10.1029/2005JD006834>
- Gent, P. R., Danabasoglu, G., Donner, L. J., Holland, M. M., Hunke, E. C., Jayne, S. R., et al. (2011). The Community Climate System Model, version 4. *Journal of Climate*, *24*(19), 4973–4991. <https://doi.org/10.1175/2011JCLI4083.1>
- Gu, Y., Liou, K. N., Lee, W.-L., & Leung, L. R. (2012). Simulating 3-D radiative transfer effects over the Sierra Nevada Mountains using WRF. *Atmospheric Chemistry and Physics*, *12*(20), 9965–9976. <https://doi.org/10.5194/acp-12-9965-2012>
- Kato, S., Rose, F. G., Rutan, D. A., Thorsen, T. J., Loeb, N. G., Doelling, D. R., et al. (2018). Surface irradiances of Edition 4.0 Clouds and the Earth's Radiant Energy System (CERES) Energy Balanced and Filled (EBAF) Data Product. *Journal of Climate*, *31*(11), 4501–4527. <https://doi.org/10.1175/JCLI-D-17-0523.1>

- Lawrence, D. M., Oleson, K. W., Flanner, M. G., Thornton, P. E., Swenson, S. C., Lawrence, P. J., et al. (2011). Parameterization improvements and functional and structural advances in version 4 of the community land model. *Journal of Advances in Modeling Earth Systems*, 3, M03001. <https://doi.org/10.1029/2011MS000045>
- Lee, W.-L., Gu, Y., Liou, K. N., Leung, L. R., & Hsu, H.-H. (2015). A global model simulation for 3-D radiative transfer impact on surface hydrology over Sierra Nevada and Rocky Mountains. *Atmospheric Chemistry and Physics*, 15(10), 5405–5413. <https://doi.org/10.5194/acp-15-5405-2015>
- Lee, W.-L., Liou, K. N., & Hall, A. (2011). Parameterization of solar fluxes over mountain surfaces for application to climate models. *Journal of Geophysical Research*, 116, D01101. <https://doi.org/10.1029/2010JD014722>
- Lee, W.-L., Liou, K. N., & Wang, C.-c. (2013). Impact of 3-D topography on surface radiation budget over the Tibetan Plateau. *Theoretical and Applied Climatology*, 113(1-2), 95–103. <https://doi.org/10.1007/s00704-012-0767-y>
- Li, J.-L. F., Lee, W.-L., Yu, J.-Y., Hulley, G., Fetzer, E., Chen, Y.-C., & Wang, Y.-H. (2016). The impacts of precipitating hydrometeors radiative effects on land surface temperature in contemporary GCMs using satellite observations. *Journal of Geophysical Research: Atmospheres*, 121, 67–79. <https://doi.org/10.1002/2015JD023776>
- Lin, S. J. (2004). A “vertically Lagrangian” finite-volume dynamical core for global models. *Monthly Weather Review*, 132(10), 2293–2307. [https://doi.org/10.1175/1520-0493\(2004\)132<2293:AVLFDC>2.0.CO;2](https://doi.org/10.1175/1520-0493(2004)132<2293:AVLFDC>2.0.CO;2)
- Liou, K. N., Gu, Y., Leung, L. R., Lee, W.-L., & Fovell, R. G. (2013). A WRF simulation of the impact of 3-D radiative transfer on surface hydrology over the Rocky Mountains and Sierra Nevada. *Atmospheric Chemistry and Physics*, 13(23), 11,709–11,721. <https://doi.org/10.5194/acp-13-11709-2013>
- Liou, K. N., Lee, W.-L., & Hall, A. (2007). Radiative transfer in mountains: Application to TP. *Geophysical Research Letters*, 34, L23809. <https://doi.org/10.1029/2007GL031762>
- Liou, K. N., Takano, Y., He, C., Yang, P., Leung, L. R., Gu, Y., & Lee, W.-L. (2014). Stochastic parameterization for light absorption by internally mixed BC/dust in snow grains for application to climate models. *Journal of Geophysical Research: Atmospheres*, 119, 7616–7632. <https://doi.org/10.1002/2014JD021665>
- Molnar, P., England, P., & Martinod, J. (1993). Mantle dynamics, uplift of TP and the Indian monsoon. *Reviews of Geophysics*, 31, 357–396. <https://doi.org/10.1029/93RG02030>
- Qiu, J. (2008). China: The third pole. *Nature*, 454(7203), 393–396. <https://doi.org/10.1038/454393a>
- Ramanathan, V., & Downey, P. (1986). A nonisothermal emissivity and absorptivity formulation for water vapor. *Journal of Geophysical Research*, 81, 8649–8666. <https://doi.org/10.1029/JD091iD08p08649>
- Su, F., Duan, X., Chen, D., Hao, Z., & Cuo, L. (2013). Evaluation of the global climate models in the CMIP5 over TP. *Journal of Climate*, 26(10), 3187–3208. <https://doi.org/10.1175/JCLI-D-12-00321.1>
- Taylor, K. E., Stouffer, R. J., & Meehl, G. A. (2012). An overview of CMIP5 and the experiment design. *Bulletin of the American Meteorological Society*, 93(4), 485–498. <https://doi.org/10.1175/BAMS-D-11-00094.1>
- Wei, Z., & Dong, W. (2015). Assessment of simulations of snow depth in the Qinghai-Tibetan Plateau using CMIP5 multi-models. *Arctic, Antarctic, and Alpine Research*, 47(4), 611–625. <https://doi.org/10.1657/AAAR0014-050>
- Willmott, C. J., & Matsuura, K. (1995). Smart interpolation of annually averaged air temperature in the United States. *Journal of Applied Meteorology*, 34(12), 2577–2586. [https://doi.org/10.1175/1520-0450\(1995\)034<2577:SIOAAA>2.0.CO;2](https://doi.org/10.1175/1520-0450(1995)034<2577:SIOAAA>2.0.CO;2)
- Wu, G., Liu, Y., Dong, B., Liang, X., Duan, A., Bao, Q., & Yu, J. (2012). Revisiting Asian monsoon formation and change associated with Tibetan Plateau forcing: I. Formation. *Climate Dynamics*, 39(5), 1169–1181. <https://doi.org/10.1007/s00382-012-1334-z>
- Wu, G., Liu, Y., Wang, T., Wan, R., Liu, X., Li, W., et al. (2007). The influence of the mechanical and thermal forcing of TP on the Asian climate. *Journal of Hydrometeorology*, 8(4), 770–789. <https://doi.org/10.1175/JHM609.1>
- Yanai, M., & Wu, G. (2006). Effects of TP. In B. Wang (Ed.), *The Asian monsoon* (pp. 513–549). Berlin: Springer.
- Zhao, H., & Moore, G. W. K. (2004). On the relationship between Tibetan snow cover, TP monsoon and the Indian summer monsoon. *Geophysical Research Letters*, 31, L14204. <https://doi.org/10.1029/2004GL020040>